

Non-close-packed plasmonic Bravais lattices through a fluid interface-assisted colloidal assembly and transfer process

Déborah Feller, Marius Otten, Michael S. Dimitriyev & Matthias Karg

Article - Version of Record

Suggested Citation:

Feller, D., Otten, M., Dimitriyev, M. S., & Karg, M. (2024). Non-close-packed plasmonic Bravais lattices through a fluid interface-assisted colloidal assembly and transfer process. Colloid and Polymer Science, 303(9), 1829–1842. https://doi.org/10.1007/s00396-024-05285-4

Wissen, wo das Wissen ist.



This version is available at:

URN: https://nbn-resolving.org/urn:nbn:de:hbz:061-20251027-114201-9

Terms of Use:

This work is licensed under the Creative Commons Attribution 4.0 International License.

For more information see: https://creativecommons.org/licenses/by/4.0

RESEARCH



Non-close-packed plasmonic Bravais lattices through a fluid interfaceassisted colloidal assembly and transfer process

Déborah Feller¹ · Marius Otten¹ · Michael S. Dimitriyev² · Matthias Karg¹

Received: 22 February 2024 / Revised: 18 June 2024 / Accepted: 20 June 2024 / Published online: 23 July 2024 © The Author(s) 2024

Abstract

The assembly of colloids at fluid interfaces followed by their transfer to solid substrates represents a robust bottom-up strategy for creating colloidal monolayers over large, macroscopic areas. In this study, we showcase how subtle adjustments in the transfer process, such as varying the contact angle of the substrate and controlling deposition speed and direction, enable the realization of all five two-dimensional Bravais lattices. Leveraging plasmonic core—shell microgels as the building blocks, we successfully engineered non-close-packed plasmonic lattices exhibiting hexagonal, square, rectangular, centered rectangular, and oblique symmetries. Beyond characterizing the monolayer structures and their long-range order, we employed extinction spectroscopy alongside finite difference time domain simulations to comprehensively investigate and interpret the plasmonic response of these monolayers. Additionally, we probed the influence of the refractive index environment on the plasmonic properties by two methods: first, by plasma treatment to remove the microgel shells, and second, by overcoating the resulting gold nanoparticle lattices with a homogeneous refractive index polymer film.

Keywords Core–shell microgels · 2-dimensional Bravais lattices · Fluid interface-assisted self-assembly · Localized surface plasmon resonance · Plasmon resonance coupling

Introduction

Fluid interface-assisted assembly of colloidal particles is a powerful method for the preparation of periodic colloidal assemblies [1–4]. Colloids tend to adsorb to fluid interfaces where they are energetically trapped and can self-assemble into ordered arrangements. These arrangements can be transferred from the fluid interface to solid substrates for applications in optics [5, 6], photonics [7], and lithography [8, 9]. Conventionally, incompressible particles such as silica or polystyrene particles are used for these processes [10–13]. By varying different parameters such as the amount of particles applied to the interface or by reducing the interfacial area in a Langmuir trough setup, one can obtain either nonclose-packed or close-packed ordered monolayers [2, 14].

Matthias Karg karg@hhu.de

The typical equilibrium structure of such monolayers is the hexagonal lattice where each colloid is surrounded by six neighbors at equal distances. When the particles are densely packed and the monolayer is further compressed, the rigidity of the particles will induce the collapse of the monolayer.

Recently, Hummel et al. have shown that any of the possible two-dimensional (2D) Bravais lattices can be prepared using fluid interface-assisted colloidal assembly of rigid and non-deformable colloids [15]. Starting from the hexagonally ordered equilibrium structure at the liquid interface, the final monolayer structure could simply be controlled by the contact angle of the solid substrate applied to transfer the monolayer from the liquid to the solid interface. The observed structures resulted, basically, as a consequence of uniaxial deformation of the close-packed monolayer during transfer to the solid substrates.

In contrast to assemblies of rigid colloids at fluid interfaces, soft and deformable particle-like objects such as poly(*N*-isopropylacrylamide) (PNIPAM) microgels [16] allow for compression over a wide range of packing fractions [17–20]. Such microgels can laterally stretch out or be compressed at the interface to interfacial dimensions much larger or much smaller than their dimensions in



Institut für Physikalische Chemie I: Kolloide und Nanooptik, Heinrich-Heine-Universität Düsseldorf, Universitätsstr. 1, 40225 Düsseldorf, Germany

Department of Materials Science and Engineering, Texas A&M University, College Station TX 77843, USA

bulk, respectively [21]. The same behavior is observed for core–shell (CS) microgels with rigid, non-deformable cores and soft microgel shells that ultimately allow for the preparation of functional periodic nanoparticle arrays [22–25]. While the microgel shell facilitates the assembly at fluid interfaces, it also acts as a spacer that can control the periodicity of assembled nanoparticle arrays [26].

In this work, we build upon our previous study of the preparation of all possible two-dimensional (2D) Bravais lattices from rigid colloids [15] and demonstrate applicability for soft and deformable, colloid-like objects. Our approach involves the utilization of deformable CS microgels containing gold nanoparticle (AuNP) cores, which undergo self-assembly at air/water interfaces. The resulting monolayer, comprised of microgels arranged in a hexagonal lattice, is then transferred onto glass substrates modified with various surface properties.

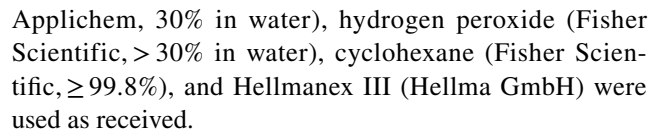
By carefully controlling the contact angle of the substrate and the direction and speed of deposition, we achieve precise control over the structure of the resulting substrate-supported colloidal monolayer. Rapid drying of the thin film leads to the formation of all possible 2D Bravais lattices, characterized by large domain sizes and a non-close-packed arrangement of dried CS microgels. Subsequent plasma treatment allows for the transformation of these lattices into non-close-packed arrangements of bare AuNPs, demonstrating the versatility of our method.

Furthermore, we demonstrate additional structural control by varying the shell sizes of the CS microgels, which enables us to adjust the lattice period. Finally, we investigate the plasmonic response of the different lattices using UV–Vis spectroscopy. This work highlights the adaptability of our transfer protocol, originally developed for uniaxially deforming hexagonally ordered monolayers of rigid colloids at fluid interfaces, to not only soft colloid-like objects but also multifunctional hybrid systems containing plasmonic NP cores.

Experimental section

Materials

Gold(III) chloride trihydrate (HAuCl₄ · 3H₂O; Sigma-Aldrich, \geq 99.999%), sodium citrate dihydrate (Sigma-Aldrich, \geq 99%), sodium dodecyl sulfate (SDS; Sigma-Aldrich, p.a.), butenylamine hydrochloride (BA; Sigma-Aldrich, 97%), N,N'-methylenebisacrylamide (BIS; Sigma-Aldrich, \geq 99%), potassium peroxodisulfate (PPS; Sigma-Aldrich, \geq 99%), cetyltrimethylammonium chloride (CTAC; Sigma-Aldrich, 25 wt% in water), ascorbic acid (Roth, p.a.), 3-(Trimethoxysilyl)propylmethacrylate (MPS; Aldrich, 98%), 1H,1H,2H,2H-Perfluorooctyltriethoxysilane (FOCTS; J&K Scientific, 97%), ethanol (Honeywell, p. a.), 1,4-dioxane (p.a., Fisher Chemicals), ammonia (PanReac



N-isopropylacrylamide (NIPAM; TCI, > 98.0%) was recrystallized from cyclohexane.

Milli-Q water (Millipore, resistivity > 18 M Ω cm) was used for all synthesis and self-assembly procedures.

Synthesis

Synthesis of gold seeds

Gold nanoparticles (AuNP seeds) were synthesized via the well-known Turkevich method [27]. In brief, 500 mL of aqueous $\mathrm{HAuCl_4} \cdot 3\mathrm{H_2O}$ (0.5 mM) were brought to heavy boiling under stirring. Twenty-five milliliters of a hot aqueous solution of sodium citrate dihydrate (1 wt%) was quickly added. The color of the reaction medium changed from light yellow to grey, black, and then to deep red. Heating was continued for a further 20 min while stirring. Afterward, the dispersion was allowed to cool down to room temperature.

Following the protocol of Rauh et al. [28], 3 mL of an aqueous SDS solution (1 mM) was added while stirring the dispersion at room temperature to increase the colloidal stability. After 20 min, 1.63 mL of an ethanolic BA solution (1.4 mM) was added to functionalize the surface of the AuNP seeds. The dispersion was left to stir for another 20 min and then concentrated by centrifugation at 1000 rcf for 16 h to yield a total of 30 mL AuNP seed dispersion.

Synthesis of CS microgels

Au-PNIPAM CS microgels were synthesized by seeded precipitation polymerization [28]. For this, the BA-functionalized AuNPs were used as seeds. In brief, NIPAM (0.588 g, 5.20 mmol) and BIS (0.134 g, 0.87 mmol) as chemical crosslinker were dissolved in 100 mL of Milli-Q water and then degassed with argon at 70 °C. After 1 h, 5 mL of the dispersion of the functionalized AuNP seeds ($c(Au^0) = 4.55$ mM) was added. Degassing was continued for 30 min. The polymerization was initiated by adding 2.2 mg of PPS dissolved in 1 mL of water. When the reaction mixture became turbid, the reaction was continued for 4 h. After cooling down to room temperature, the CS microgels were purified by three consecutive centrifugation steps, each at 9400 rcf for 1 h. After the first two steps/the last step, the residue was redispersed in 30 mL/15 mL of water, respectively. The Au-PNIPAM microgels were then freeze-dried for 3 days. The description of the synthesis details of larger Au-PNIPAM microgels can be found in the Supplementary Information.



In situ overgrowth of the gold cores

The overgrowth protocol used to increase the size of the spherical gold cores was adapted from Ponomareva et al. [23]. Briefly, an aqueous solution of Au-PNIPAM microgels (4.68 wt%) was mixed with an aqueous CTAC solution (10 mM) in a 1:1 volume ratio. Eight hundred microliter of this dispersion was added to 32 mL of an aqueous CTAC solution (2.4 mM) while stirring in an Erlenmeyer flask. One overgrowth step consisted of the addition of 624 µL of an aqueous ascorbic acid solution (49 mM) in one shot followed by the dropwise addition of 48 mL of an aqueous solution containing CTAC (6.2 mM) and HAuCl₄ · 3H₂O (0.5 mM). The overgrowth process was allowed to proceed for 30 min while slow stirring. The overgrowing procedure required seven steps to reach core sizes of about 100 nm in diameter. This was followed by UV-Vis spectroscopy after each step in order to reach a localized surface plasmon resonance (LSPR) maximum at about 580 nm. After the seventh growth steps, the reaction medium was stirred overnight. The final CS microgels were then dialyzed against water for 4 days with water exchange twice a day. After the dialysis, the microgels were centrifuged three times for 30 min at 5400 rcf. After each step, the final residue was dispersed in 600 µL of ethanol.

Hydrophobization of glass substrates

Glass substrates $(2.4\times2.4~\text{cm}^2)$ were cleaned by sonification in an aqueous solution of Hellmanex III (2 vol%), followed by water and then ethanol for 15 min each. Afterward, the substrates were dried with a stream of compressed N_2 resulting in hydrophilic substrates with a contact angle of 15°. A clean substrate was then placed on a spin-coater, and 40 μ L of a PS solution (1 wt% in 1,4-dioxane, 120,000 g/mol) was placed in the middle of the substrate. Spin-coating was performed at 2000 rpm for 20 s resulting in a hydrophobic substrate with a contact angle of 96°.

Prior to the functionalization of glass substrates with FOCTS and MPS, glass substrates ($2.4 \times 2.4 \text{ cm}^2$) were cleaned by the RCA-1 method [29]. Five parts of water were mixed with one part of ammonia (30%) and heated to 80 °C while stirring. When the temperature of the solution was constant, one part of H_2O_2 (30%) was added. Glass substrates were immersed into the solution for 15 min when the temperature was between 75 and 85 °C. Afterward, the glass substrates were rinsed thoroughly with water and left in water for 5 min before drying in a stream of compressed N_2 .

The functionalization of the glass substrates was done using chemical vapor deposition. Therefore, the substrates were placed in a desiccator with 120 μ L of the functionalizing agent (FOCTS or MPS), and the pressure was reduced to 150 mbar. The functionalization was allowed to proceed

overnight. The glass substrates were then removed and baked at 60 °C in an oven for 2 h. After the baking process, the substrates were sonicated for 10 min in ethanol and then dried with N_2 . This procedure resulted in hydrophobic substrates with a contact angle of 114° for FOCTS and 87° for MPS, respectively.

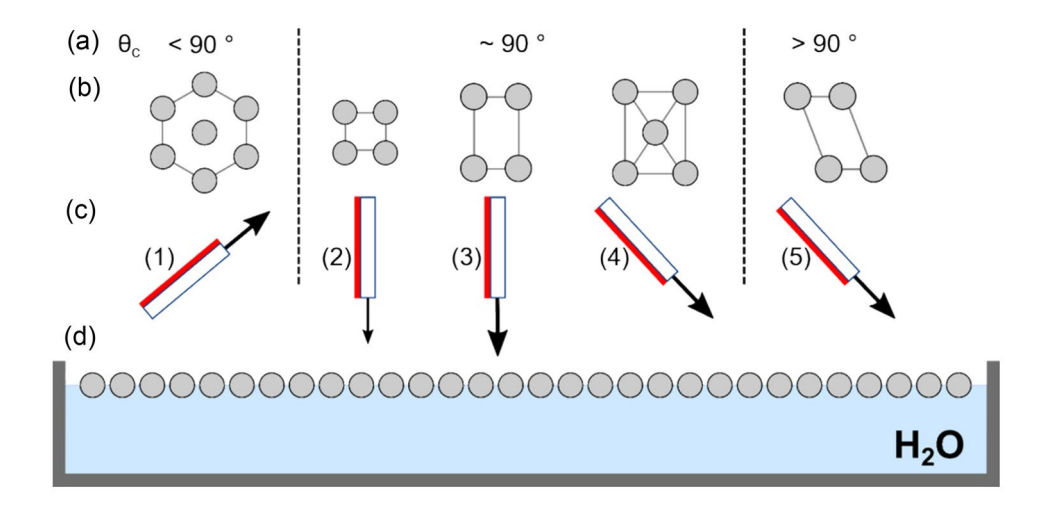
Contact angles were measured with the drop shape analyzer Krüss DSA 25 by applying a droplet of $10 \,\mu\text{L}$ of Milli-Q water on the functionalized substrates.

Monolayer preparation and transfer

The preparation process to obtain the different Bravais lattices is schematically shown in Scheme 1. The process is inspired by the one reported by Hummel et al. for rigid spheres [15] and uses the assembly of freely floating monolayers in a crystallizing dish instead of using a Langmuir trough. In other words, for the current preparation, we cannot control the degree of compression, i.e., the total accessible interfacial area, and thereby we cannot control the packing fraction. For the freely floating monolayers, we expect surface pressures to be low and interparticle distances to be large as we will later confirm in the Results and Discussion section. While our aim here was to follow the process from the literature and provide an easy, low-tech preparation scheme, for future work, it might be interesting to perform such experiments at different states of monolayer compression.

A crystallizing dish was filled with Milli-Q water and 7 μL of the Au-PNIPAM microgels dispersed in ethanol were carefully injected directly to the air/water interface, where the microgels self-assembled into a freely floating monolayer (Scheme 1d). Depending on the targeted Bravais lattice (Scheme 1b), different transfer geometries (Scheme 1c) and contact angles of the substrates (Scheme 1a) were used. The hexagonally ordered structure was prepared by using a hydrophilic substrate (θ <90°) according to the protocol of Volk et al. . Here, the substrate was immersed in the bulk water phase vertically and then placed below the monolayercovered air/water interface. By retracting the substrate through the monolayer at a shallow angle, the monolayer was transferred from the interface to the substrate. The sample was dried with a heat gun by blowing warm air from below the glass substrate (uncovered side). The other four lattices were prepared by adapting the protocol of Hummel et al. [15]. Hydrophobic substrates with a contact angle of 96° for square, 87° for rectangular and centered rectangular, and 114° for oblique structures were used. In order to transfer the monolayer from the interface to the glass substrates, the substrates were immersed through the monolayer into the bulk phase. For the square lattice, the substrate was immersed vertically at a rather slow speed of 15 mm/s using





Scheme 1 Schematical depiction of the preparation method for the five different Bravais lattices. The Au-PNIPAM microgels are represented by grey circles (oversimplified). **a** The contact angle θ_c of the substrates can be divided into three ranges. **b** Structural illustration of the five different Bravais lattices. **c** Illustration of the retraction/immersion procedure to immobilize the assembled particles on the red-colored side of the substrates. (1) Retraction of monolayer at a

shallow angle. (2), (3) Vertical immersion of the substrate through the monolayer. (4), (5) Immersion at a shallow angle through the monolayer. The thickness of the arrow illustrates the retraction/immersion speed. Contact angles of the substrate used in the experiment are (1) 15° , (2) 96° , (3) 87° , (4) 87° , and (5) 114° , respectively. **d** Crystallizing dish with particles assembled into a monolayer at the air/water interface

a dip-coater. For the rectangular structure, the glass was immersed vertically and significantly faster by hand. It is important to note that the square lattices were only obtained at the slow transfer speed with the best results using a dipcoater, while the manual transfer for the rectangular structure had to be performed significantly faster and was found more robust against variation in the transfer speed. The centered rectangular structure, as well as the oblique structure were received by immersing the respective substrate through the monolayer at a shallow angle. For all cases, where the substrate was pushed through the monolayer for the transfer, the substrates were placed at the bottom of the crystallizing dish with the monolayer facing up. The substrates were then thermally annealed for 10 min by placing the crystallizing dish on a hotplate at 130 °C in order to increase the adhesion of the monolayer to the substrate. Then the glass substrates were removed and dried with a heat gun from underneath.

Plasma treatment of the substrate-supported monolayers

In order to remove the microgel shell of the Au-PNIPAM monolayers on the glass substrates, plasma treatment was performed for 45 min at 300 W in an oxygen atmosphere using PlasmaFlecto 10 (plasma technology GmbH). Afterward, the glass substrates were washed with Milli-Q water to remove any polymeric residues and dried in a stream of compressed N_2 .

Superstrate coating of the AuNP monolayers

In order to embed the substrate-supported AuNP monolayers (after plasma treatment) in a homogenous refractive index environment, linear PNIPAM homopolymer (85,000 g/mol, synthesized via the protocol by Ebeling and Vana [30]) was spin-coated on top of the monolayer. To accomplish this, 60 μ L of linear PNIPAM solution (5 wt% in 1,4-dioxane) was placed in the middle of the glass substrate. Spin-coating was then performed at 2000 rpm for 60 s resulting in a homogeneous polymer film with a thickness of 1.5 μ m as determined by atomic force microscopy (AFM).

Methods

Transmission electron microscopy (TEM)

TEM was used to examine the morphology of the CS microgels and to verify the success of the polymer encapsulation of the AuNP cores. Imaging was performed with a JEOL JEM-2100Plus TEM in bright-field mode operated with an acceleration voltage of 80 kV. The samples were prepared on carbon-coated copper grids (200 mesh, Electron Microscopy Science) by drop-casting 7 μ L of a dilute aqueous Au-PNIPAM microgel dispersion. The grids were dried at room temperature for 1 h. Core sizes were measured using the software ImageJ [31].



Atomic force microscopy (AFM)

AFM height images were recorded in intermittent contact mode against air with a Nanowizard 4 (JPK Instruments). The images were recorded with an OTESPA-R3 AFM probe (Bruker). The tip geometry was a visible apex with a nominal tip radius of 7 nm. According to the manufacturer, the cantilever possesses a resonance frequency of 300 kHz and a spring constant of 26 N/m. Exact values were not measured. The recorded images of $20\times20~\mu\text{m}^2$ had a resolution of $1024\times1024~\text{pixel}^2$. The software ImageJ was used to analyze the images and to create the FFT, as well as the autocorrelation images [31].

UV-vis spectroscopy

Extinction spectra were recorded using a Specord S 600 UV–Vis spectrophotometer (Analytik Jena AG) in the wavelength range of 250–1019 nm. The spectra of dilute samples were measured in transmission geometry using 1 cm PMMA cuvettes. Coated glass substrates were held upright in the light path with the particle monolayer facing toward the detector. Cuvettes with water or clean glass substrates were used as reference, respectively. The PNIPAM-coated monolayers were also background corrected with a clean glass substrate, as there was no detectable difference between clean glass and PNIPAM-coated glass (see Fig. S14).

Scanning electron microscopy (SEM)

SEM images were recorded with a ZEISS SUPRA 55VP equipped with a field emission gun (FEG). The instrument was operated at acceleration voltages of 10 and 20 kV. The images were recorded with either a secondary electron (SE2) or an angle-selective backscattered (AsB) detector. The AsB detector enhanced the material contrast making it possible to visualize the cores in the PNIPAM shell. Prior to the measurements, the samples were sputtered with a layer of gold to enhance the conductivity.

Finite difference time domain (FDTD) simulations

Extinction spectra of the five Bravais lattices were calculated with the finite difference time domain (FDTD) method. The calculation software is commercially available from Lumerical Solutions, Inc. (FDTD Solutions, Version 8.18.1332). We simulated the spectra for finite-size lattices in a box with perfectly matched layer (PML) boundary conditions in all three spatial directions. A total-field scattered-field source with incident wavelengths of 290–910 nm was used. Two boxes of power monitors, one in the total field region and one in the scattered field region were used to calculate the absorption and the scattering. The lattices were constructed

with a domain size of three for all five structures. The size of the dried CS microgels was estimated from the AFM height image by taking the full-width half maximum of a cross-section from a dried CS microgel as the diameter. Core sizes were determined from TEM images. The interparticle distances in the different Bravais lattices for the comparison between experiment and simulation were taken from the experimental AFM height images. For the calculated extinction spectra of the Bravais lattices with the same period, we choose to use a period of 350 nm, which was close to the experimental period of the square lattice. As the refractive index (RI) of gold is wavelength-dependent, values from the literature were taken [32]. The PNIPAM shell of the microgels was simulated with a RI of 1.49 [33], which is slightly smaller than 1.50 known from Brasse et al. [34] to account for the residual water content in the shell. The air background and the glass substrate were simulated with a RI of 1 and 1.52, respectively. Uniform meshes of 2.5 nm (centered rectangular), 3.5 nm (square), 4 nm (hexagonal and rectangular), and 7.5 nm (oblique) were used in the area of the lattice in addition to a nonuniform mesh. The auto shut-off of the calculation was set to 10^{-5} , which was already reached before a simulation time of 1000 fs.

Voronoi and Delaunay tessellations

Local order analyses of the core positions, including the generation of Voronoi and Delaunay tessellations, were performed using codes developed in Wolfram Mathematica v13.2. To exclude boundary artifacts in the tessellations, cells closest to the boundary (within 10% of the full width of the region of interest) were excluded from the analyses.

Results and discussion

Characterization of the colloidal building blocks

Similar to our previous work [23], CS microgels with single, nanocrystalline gold cores and soft, deformable PNIPAM shells were chosen as the colloidal building blocks. These hybrid microgels were synthesized via seeded precipitation polymerization followed by the controlled in situ overgrowth of the gold cores. The overgrowth of the cores can easily be tracked by UV–vis extinction spectroscopy due to the dependencies of the LSPR position and resonance strength on the core size. Figure 1a shows the normalized extinction spectra of the initial CS microgels (dark green) and of the batches after each of the seven growing steps (from green to red). The dark green curve shows the Rayleigh-Debye-Gans scattering of the PNIPAM shell which dominates the absorption of the Au core, so the LSPR peak is not visible in the spectrum [35, 36]. After the first step, the cores grow in size, and the LSPR



peak becomes visible. The maximum of the LSPR peak shifts from 542 nm and a full-width half-maximum (FWHM) of 68 nm after the first step to 581 nm and a FWHM of 88 nm after the seventh step with an increase in intensity. The LSPR peak is ascribed to a dipolar mode, which is the only mode to be expected for the size range of the cores [23].

TEM images recorded from samples before (Fig. 1b) and after (Fig. 1c) the overgrowth confirm the successful encapsulation, as well as the increase in the size of the cores in the polymer shell. The cores are nicely located in the center of the shell, which is expected for CS microgels with 16.7 mol% nominal BIS content, i.e., high crosslinker density [37]. The microgels have core diameters, $d_{\rm core}$ of 14.1 ± 1.1 nm and 98.1 ± 7.9 nm in Fig. 1b, c, respectively. The size distribution of the overgrown cores can be found in the Supporting Information Fig. S1. The hydrodynamic radius, $R_{\rm h}$, of the final microgels after the seventh step of core growth was determined as 172.9 ± 3.4 nm using dynamic light scattering (DLS) at 20 °C.

Fluid interface-assisted assembly and characteristics of the hexagonal equilibrium structure

The CS microgels were self-assembled at the air/water interface to form a freely floating monolayer of hexagonally ordered microgels as the equilibrium structure. By using the common retraction method with a hydrophilic glass substrate [25], the microgels are hexagonally ordered on the substrate as shown in Fig. 2a. In contrast to previously reported by Kuk et al. [38], we do not see any drying artifacts in our monolayer. Here, the drying effects are suppressed by the fast drying of the substrate with a heat gun. Thus, the microgels do not have sufficient time to rearrange, and the structure on the substrate is expected to resemble closely the one at the air/ water interface [39]. The AFM height image shows a highly ordered monolayer with only a few local defects in the structure. In addition, predominately one domain can be identified which confirms the long-ranging order of the monolayer over a distance of several micrometers. To further analyze

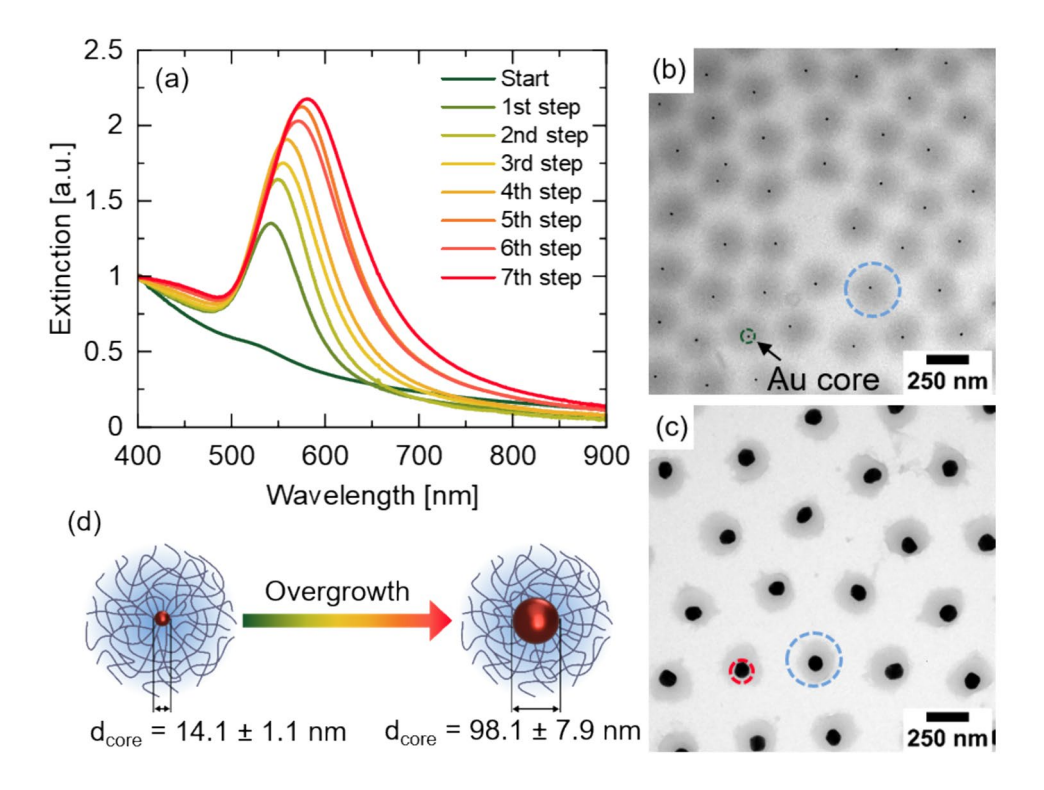


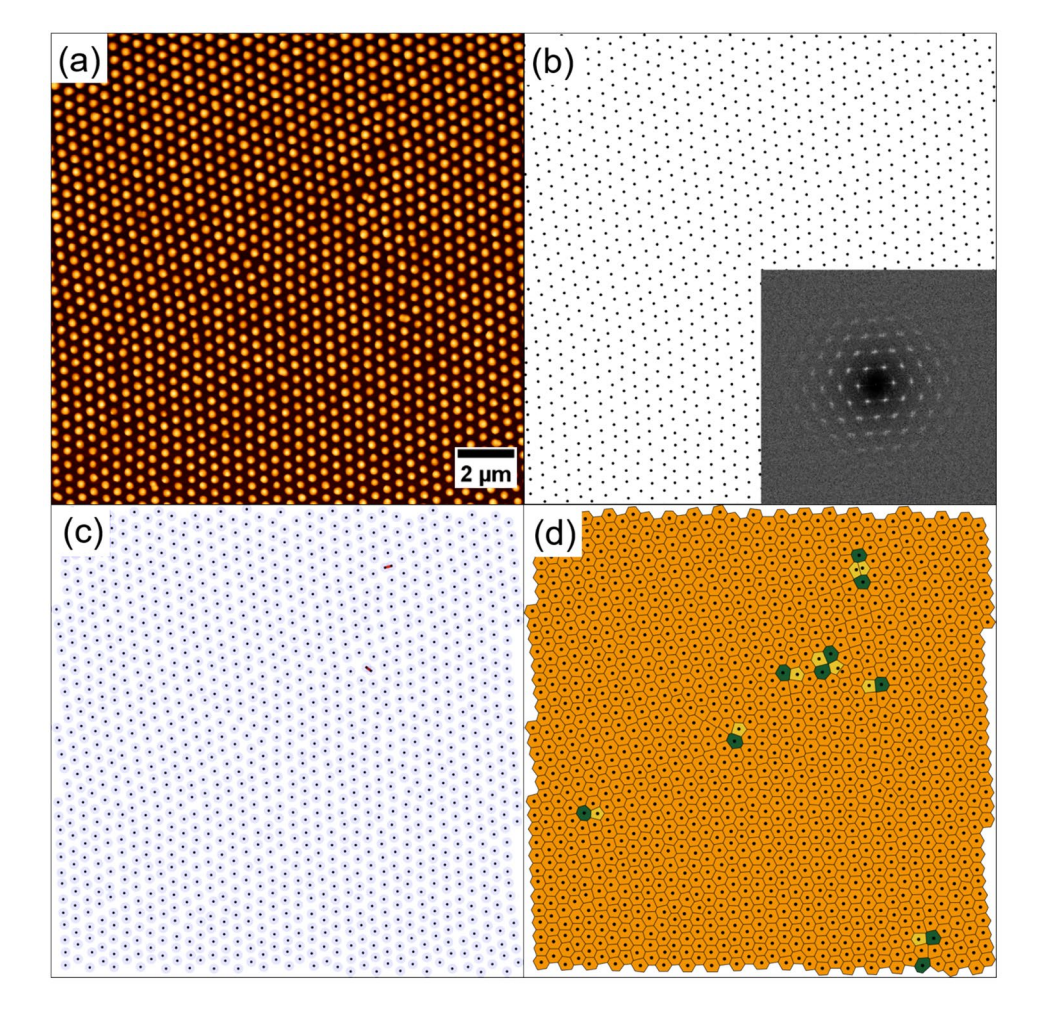
Fig. 1 Overgrowth of Au cores in the PNIPAM shell via seven-step synthesis. a Extinction spectra normalized to the extinction at 400 nm. The spectra show the evaluation of the LSPR peak over the seven overgrow steps from dark green to red. b TEM image of the Au-PNIPAM microgels prior to the core overgrowth. The Au core is highlighted by the dark green-dashed circle and the PNIPAM shell by the blue-dashed circle. c TEM image of the Au-PNIPAM microgels after

the seventh overgrow step. The overgrown Au core is highlighted by the red-dashed circle and the PNIPAM shell by the blue-dashed circle. **d** Schematical representation of Au-PNIPAM microgels before and after the overgrow synthesis with the corresponding core diameters. The color coding of the arrow corresponds to the color of the overgrowing steps in (a)



the structure and degree of order, the AFM height profile from Fig. 2a was first transformed into a point map shown in Fig. 2b. This point map shows only the center of mass of each CS microgel, which was then used to compute the fast Fourier transform (FFT) shown as inset. The FFT shows sharp Bragg peaks of several orders revealing the six-fold symmetry of the monolayer and the long-range order. In Fig. 2c, the point map approximates the configuration of the CS microgels in real space. This is done by approximating the bulk dimensions of each individual microgel to be identical, so that each microgel is distinguished by its center-of-mass coordinate. The NP cores are represented by black circles and the microgel shells as light corona with a radius of 173 nm which corresponds to the hydrodynamic radius from bulk measurements (DLS). With these dimensions, the lattice appears non-close-packed with almost all microgels being not in contact, except for two pairs of microgels, as shown by the red lines. These pairs are the result of the deformability of the microgel shells which can compensate for lattice defects. Furthermore, in the initial monolayer at the air/water interface, the shells stretch laterally into a "fried egg"-like shape occupying a larger area at the interface [40]. Thus, the diameter of the microgels at the interface is expected to be larger than the diameter in bulk which explains the high degree of order. Upon drying, the shell shrinks and particles seem to not be in contact anymore, as also suggested by the AFM height image in Fig. 2a. These findings are also confirmed by the Voronoi tessellation in Fig. 2d, generated from the point map. The majority of the microgels show a sixfold coordination (orange hexagons) with neighboring microgels, which is also expected for a hexagonal array. Some defects in the monolayer can be detected by the 5-coordinated (yellow pentagons) and by the 7-coordinated (green heptagons) microgels, often appearing as bound disclination pairs, indicative of a lattice dislocation. Nucleation sites for pairs of bound dislocations can be found at the groupings of four disclinations, consisting of a pair of 5-coordinated and a pair of 7-coordinated. While the presence of unbound dislocations indicates the potential development of a hexatic phase, the effect on the overall order of the monolayer seems to be minimal. This robustness can be rationalized by the softness of the microgels, as the shell is able to compensate for some disorder in the arrangement.

Fig. 2 Hexagonally ordered monolayer of Au-PNIPAM CS microgels. a AFM height image of the monolayer. b Point map of the center of mass of the CS microgels extracted from the AFM height images. The inset shows the FFT of the point map. c Scheme of the microgels ordered on the substrate. The black points represent the cores, and the shell is shown in light blue. The shells have a radius which corresponds to the hydrodynamic radius of nearly 173 nm. The red lines show particles which are in contact, with overlapping shells. d Voronoi tessellation generated from the point map. 6-coordinated particles are shown as orange hexagons. 5- and 7- coordinated disclination defect pairs are shown as yellow pentagons and green heptagons, respectively. Scale bar in a is representative of all four images





The freely floating monolayer with hexagonally arranged microgels with laterally stretched shells in shell-shell contact is the starting point for the preparation of the four remaining 2D Bravais lattices that will be addressed in the following.

Bravais lattices of soft CS microgels

We prepare Bravais lattices from soft microgels via a fluid interface-assisted process. The resulting lattice strongly depends on the immersion angle and speed, as well as on the contact angle of the glass substrate, as shown in Scheme 1. We want to note that in the previous work of Hummel et al. using hard spheres, the monolayer deformation was dominantly controlled via the substrate wettability affecting the ratio of flow velocity to substrate immersion velocity [15]. In the case of our microgels, we could not obtain similar results as for the rigid spheres by simply varying the substrate wettability. While we believe that the general mechanism of lattice deformation is similar and driven by the flow velocity toward the contact line, we will see that the mechanism is more complex for soft and deformable microgels where interparticle and particle-to-substrate interactions differ significantly compared to rigid spheres [38]. We immersed hydrophobic substrates through the monolayer at the interface to prepare the other four Bravais lattices, namely square, rectangular, centered rectangular, and oblique [15]. In Fig. 3, the top row shows the AFM images of the resulting five Bravais lattices. The microgels are highly ordered in predominately one domain nearly without any visible defects. The type of lattice is represented by a hexagon (a), a square (b), a rectangular (c), a centered rectangular (d), and an oblique tetragon (e), all marked in red. Larger AFM images with the corresponding FFTs and autocorrelation images of all five Bravais lattices can be found in Figs. S2, S3, S4, S5, and S6.

The middle row in Fig. 3 shows 2D autocorrelation functions computed from the AFM images shown in the top row. The autocorrelation functions not only nicely reveal the different lattice symmetries, but they also confirm the long-range order due to the large number of correlation peaks. Blurring at the edges of the autocorrelation images is due to the finite dimension of the AFM images. The length of the edges, as well as the angle of the unit cell from the Bravais lattices (shown in Fig. 3 bottom row), were determined by measuring four unit cells in the autocorrelation function. The results are listed in Table 1.

For the square structure, the lengths of the edges a and b match closely with only a 7% deviation from the mean. We want to note that the real deviation is potentially smaller because of the limited resolution of the images where one pixel corresponds to approximately 20 nm. When comparing the lengths, a and b of all structures, the hexagonal structure shows larger spacings than the square, rectangular, and oblique ones, which can be attributed to the different preparation method. The edge length a for the centered rectangular arrangement of 647 ± 2 nm is nearly the double of the edge lengths for the square arrangement. This can be explained by the period of the structure. For the square lattice, the period equals the edge length, but for the centered rectangular lattice, the period equals the half of the edge length a. Thus, we can conclude that the spacing of all prepared Bravais lattices ranges in the same magnitude. Voronoi and Delaunay tessellations of the square, rectangular, centered rectangular, and oblique lattices are provided in Figs. S7 and S8 of the Supporting Information.

Surface coverage at different substrate positions

We performed several AFM measurements on a cm²-large substrate coated with an oblique structured monolayer to

Fig. 3 Bravais lattices prepared on glass substrates with CS microgels via self-assembly at the air/water interface. The top and middle row show AFM height images and their autocorrelation images, respectively. The scale bar corresponds to 1 µm. The Bravais lattice is marked in red. The bottom row shows the different unit cells of the Bravais lattices with the corresponding lengths of the cell edges a, b, c, and d and the angles θ and φ . The five Bravais lattices: hexagonal (a), square (b), rectangular (c), centered rectangular (d), and oblique (e)

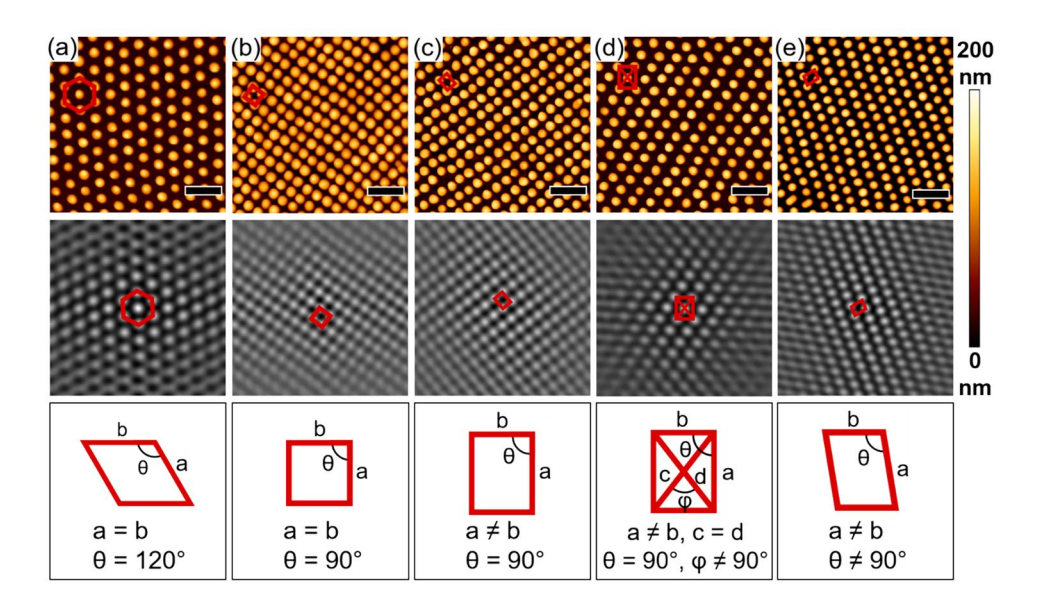




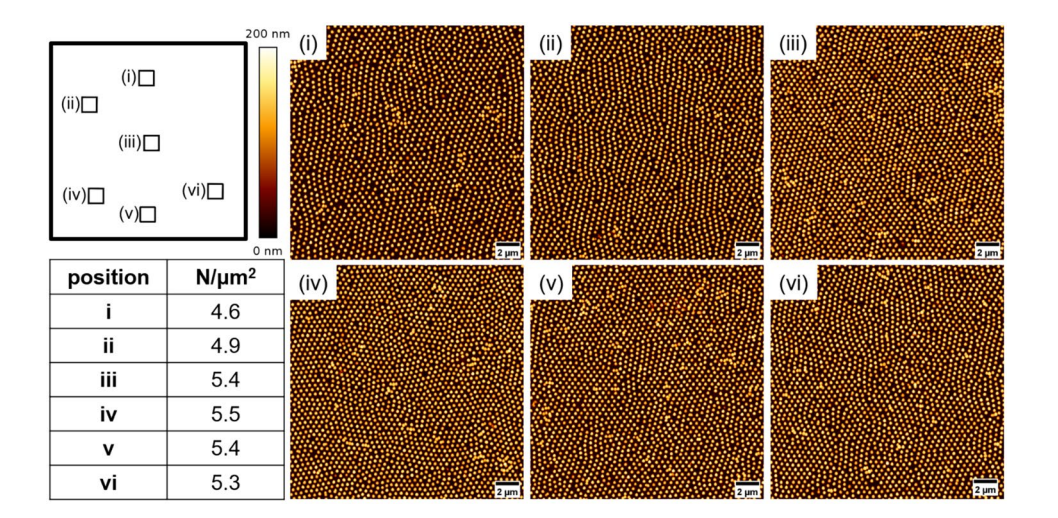
Table 1 Values of the edge lengths a and b, respectively and of the angle θ for the five Bravais lattices. Values were determined by measuring four unit cells in the autocorrelation function of the corresponding Bravais lattice

| Parameter | Hexagonal | Square | Rectangular | Centered rectangu- lar | Oblique |
|---------------|--------------|------------|-------------|------------------------------|-------------|
| a [nm] | 471 ± 15 | 353 ± 5 | 375 ± 1 | 647 ± 2 | 381 ± 2 |
| <i>b</i> [nm] | 471 ± 15 | 330 ± 1 | 324 ± 1 | 501 ± 3 | 314 ± 1 |
| θ [°] | 119 ± 2 | 89 ± 3 | 89 ± 3 | 91 ± 5 | 103 ± 1 |

confirm the homogeneity of the colloidal monolayer. In Fig. 4, six AFM height images and a schematical depiction of a substrate marked with the analyzed positions are shown. The images reveal multi-domain structures with several defects (mostly voids and local clusters). Nevertheless, the oblique symmetry of the monolayers can be identified in all images independent of the position on the glass substrate.

We determined the particle number (N) per area (in μ m²) as a measure of the surface coverage and homogeneity. For this, CS microgels were counted in each AFM image of 400 μ m² size each. The values for each position are summarized in the table shown in the bottom left of Fig. 4. On average, 5.2 ± 0.3 particles per μ m² cover the substrate. The deviation of less than 10% indicates a uniform coating and thus similar interparticle distances (d_{c-c}). Furthermore, extinction spectra at the respective positions were recorded (see Fig. S9). The average plasmon peak position is 584 ± 1 nm, and spectra show very little variation supporting the homogeneity of the monolayer. We now want to look deeper into the plasmonic response of the different monolayers.

Fig. 4 AFM height images of an oblique structured monolayer from different locations on a cm²-scale glass substrate ((i)–(vi)). Top left shows a schematical depiction of the substrate where the analyzed positions are marked by small squares. Bottom left represents a table with the number of particles (*N*) per area in μm² for the six positions. Particle numbers were determined from the AFM height images considering areas of 400 μm² each



Plasmonic properties of the Bravais lattices

The optical properties of the Bravais lattices were investigated by UV-vis extinction spectroscopy in normal transmission geometry. All five structures show single resonance peaks in the visible wavelength range that are related to the extinction of a dipolar LSPR of the AuNP cores (see Fig. 5a). The peak positions and widths vary slightly within the different samples (see also Table 2). With peak positions ranging between $\lambda_{LSPR} = 570$ nm (rectangular) and $\lambda_{\text{LSPR}} = 599 \text{ nm}$ (hexagonal), the resonances are close to the value of $\lambda_{LSPR} = 581$ nm measured in dilute dispersion. At a closer look, we find that the hexagonal lattice shows a redshifted resonance peak with respect to the spectrum from dispersion. This shift to a higher wavelength can be attributed to a slightly higher RI environment of the AuNP cores on the glass substrate and with the collapsed PNIPAM shell (dried) in between and on top of the NPs [23]. Interestingly, the other lattices show significantly blueshifted peaks with smaller peak width compared to the hexagonal lattice. We attribute these changes to long-range radiative interactions within the periodic lattices [23, 41–43]. In contrast, without such far-field interactions, given that the RI conditions are the same for all lattices, one would expect perfectly overlapping normalized spectra. This is clearly not the case.

To support our experimental findings, we performed FDTD calculations of all five Bravais lattices. We first start with results from simulations that use the same period of 350 nm independent of the lattice geometry. The simulated extinction spectra are provided in Fig. S10. In contrast to our experimental findings, the LSPR positions are significantly redshifted and show only slight variations between the different lattices (see also Table S2 in the Supporting Information). The simulated LSPR peaks lie in the range of 609 to 618 nm. In accordance with the literature, peak positions show only a slight deviation [44].

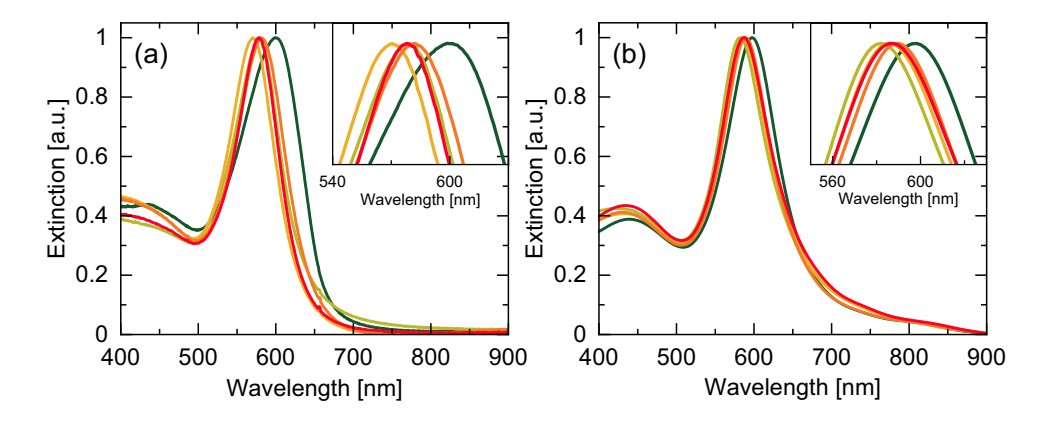


Fig. 5 Extinction spectra of the different Bravais lattices on glass substrates. Experimental (**a**) and simulated (**b**) extinction spectra of the hexagonal (dark green), square (light green), rectangular (yellow), centered rectangular (orange), and oblique lattice (red). Values of $d_{\rm c-c}$

used in the simulation were adapted from experiment. All spectra are normalized to the extinction at the respective peak maximum. The insets show a magnification of the different peak maxima

Next, we simulated extinction spectra using the experimentally determined spacings (Fig. 5b). This time the simulated resonance positions are much closer to the experimental ones. Experimental and simulated spectra generally agree well albeit slightly larger deviations in resonance position for the non-hexagonal lattices. Differences in peak position and width (see also Table 2) can be attributed to defects and limited domain sizes in the experimental samples in contrast to the defect-free, simulated lattices. We want to note that the standard extinction spectroscopy in our experiments probes large, macroscopic areas thus averaging over many domains. The direct comparison of experimental and simulated spectra of our lattices shows that the interparticle distance is the dominant parameter influencing the plasmon resonance position rather than the lattice symmetry.

Influence of lattice spacing on plasmonic response

In order to further investigate the influence of the interparticle distance on the optical response, we prepared oblique lattices using differently sized CS microgels. While these CS microgels feature similar AuNP core sizes of 98.1 ± 7.9 nm and 94.9 ± 9.8 nm, respectively, their total hydrodynamic radii are 172.9 ± 3.4 nm for the smaller and 230.2 ± 7.3 nm for the larger microgels, respectively. Due to the similar core dimensions, the LSPR positions measured from dilute

aqueous dispersion were found to be 584 nm and 588 nm for the smaller and larger microgels, respectively. TEM images, as well as extinction spectra of both batches of CS microgels can be found in the Supporting Information in Fig. S11. Figure 6a, b shows AFM height images recorded from oblique monolayers prepared from both microgel batches. Both images reveal the oblique structure with the multi-domain character and some defects. The larger microgel size and thus the lower surface coverage for the monolayer prepared from the large CS microgels can be clearly seen in Fig. 6b as compared to 6a. The edge lengths a and b, as well as the angle θ were measured from autocorrelation images, and the corresponding values are listed in the table in the bottom right of Fig. 6. As expected, the edge lengths increase with the total size of the microgels.

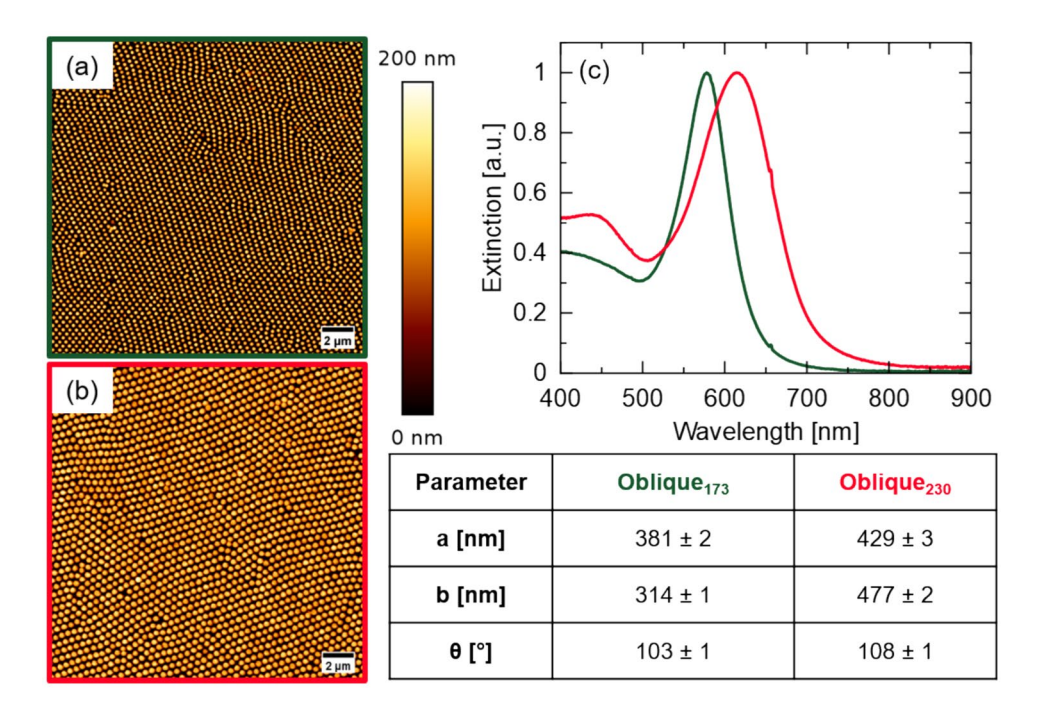
The extinction spectra of both monolayers are depicted in Fig. 6c. Both spectra show single plasmon resonance peaks in the orange to the red part of the visible spectrum, i.e., close to 600 nm wavelength. The direct comparison of the spectra reveals a significantly redshifted resonance with higher FWHM for the lattice prepared from the larger CS microgels (red spectrum), i.e., the lattice with larger interparticle spacings. For that sample long-range electromagnetic coupling—if present—is expected to be significantly lower than for the sample with the smaller lattice spacing. Thus, the latter experiments not only underline the relevance

Table 2 Wavelength of the LSPR peak maximum (λ_{LSPR}) for the five Bravais lattices in the experiment (Exp) and the corresponding simulation (Sim). Full width half maximum (FWHM) of the LSPR peak for the five Bravais lattices in the experiment and the corresponding simulation

| | Hexago | Hexagonal | | Square | | Rectangular | | Centered rectangular | | Oblique | |
|-----------------------|--------|-----------|-----|--------|-----|-------------|-----|----------------------|-----|---------|--|
| | Exp | Sim | Exp | Sim | Exp | Sim | Exp | Sim | Exp | Sim | |
| λ_{LSPR} [nm] | 599 | 597 | 578 | 583 | 570 | 586 | 581 | 589 | 578 | 587 | |
| FWHM [nm] | 88 | 66 | 59 | 58 | 62 | 58 | 66 | 57 | 56 | 61 | |



Fig. 6 Variation of an oblique structured monolayer by using particles with different $R_{\rm h}$. AFM height images of an oblique structured monolayer prepared with particles with $R_{\rm b} = 172.9 \pm 3.4 \text{ nm}$ (a) and $R_{\rm h} = 230.2 \pm 7.3 \text{ nm } (\mathbf{b}), \text{ respec-}$ tively. c Extinction spectra of the two monolayers. Extinction spectra normalized to the extinction at the respective peak maximum. Bottom right shows a table with values of the edge lengths a and b, respectively, and of the angle θ for the two monolayers. Values were determined by measuring four unit cells in the autocorrelation function of the corresponding monolayer. The subscripted numbers indicate the hydrodynamic radius R_h of the CS microgels

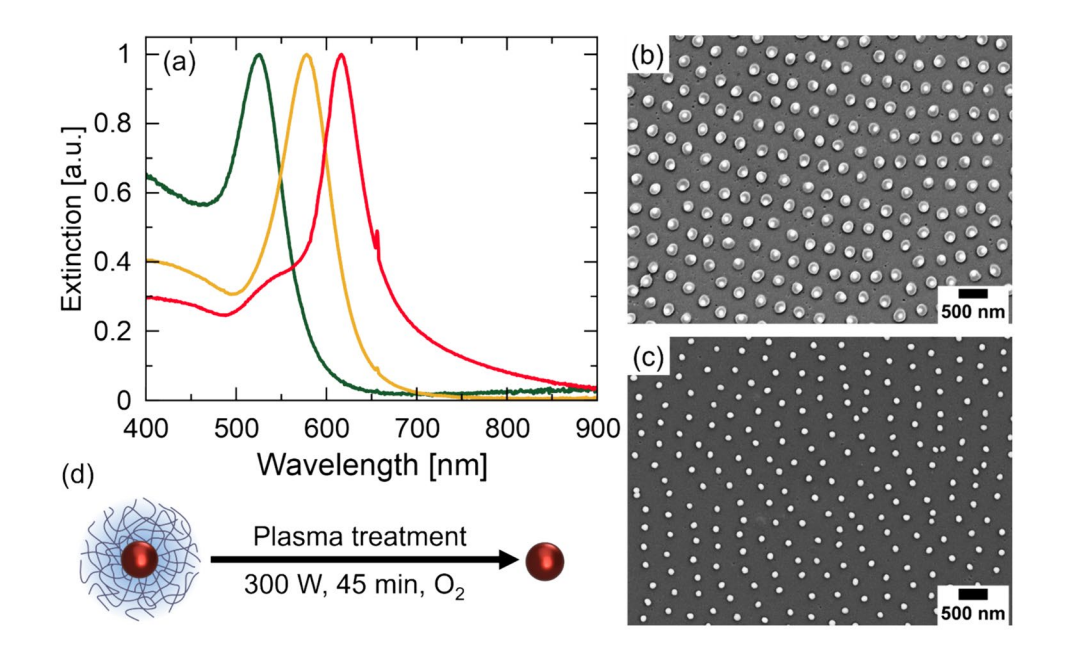


of the interparticle distance on the optical response of the monolayers but also support the versatility of our assembly protocol that can be applied successfully to differently sized microgels. Generally, due to the rather large dimensions of the microgel shells as compared to the much smaller inorganic cores, we believe that the colloidal assembly is determined by shell-shell interactions with little to zero influence of the cores. Thus, our protocol will not be limited to Au-PNIPAM CS microgels, meaning that also non-close-packed 2D Bravais lattices of other nanoparticles will be accessible.

Influence of the superstrate on plasmonic response

In order to study the influence of the RI environment and the homogeneity of the superstrate, we performed different post-modifications to an oblique lattice and followed the changes in the optical response. In all cases, glass is the underlying substrate, and measurements were performed in standard transmission geometry. Figure 7a compares normalized extinction spectra where the spectrum in yellow corresponds to the as-prepared lattice of the CS microgels. For that sample, the AuNP cores are embedded in anisotropic

Fig. 7 Post-treatment of an oblique lattice. a Normalized extinction spectra of the asprepared lattice of Au-PNIPAM CS microgels (yellow), of the resulting AuNP lattice after plasma treatment (green), and of the plasma-treated lattice after coating with a homogenous PNIPAM film as superstrate (red). SEM images of the asprepared lattice of CS microgels (b) and of the resulting AuNP lattice after plasma treatment (c). SEM images were recorded with an angle-selective backscattered electron detector (b) and a secondary electron detector (c). d Schematical depiction of the plasma treatment step to remove the PNIPAM shell





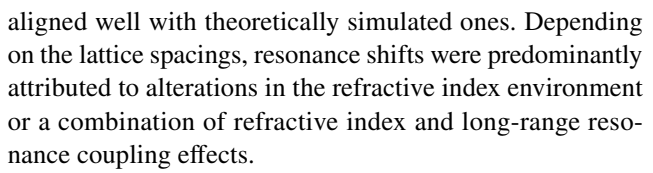
shells of dried PNIPAM with some residual water [33], and the superstrate is air. This inhomogeneous RI environment results in a resonance peak at $\lambda_{LSPR} = 578$ nm with a peak width of 56 nm (FWHM). Figure 7b shows the corresponding SEM image of the sample. By plasma treatment, the PNI-PAM can be removed as shown by the SEM image in Fig. 7c and schematically illustrated in Fig. 7d. Additional SEM images before and after plasma treatment can be found in the Supporting Information (Figs. S12 and S13). In Fig. 7a, the spectrum in green shows the optical response of the plasmatreated sample with a significantly blueshifted resonance at 524 nm with a peak width of 60 nm (FWHM). The blueshift can be explained by a decrease of the effective RI due to the removal of the PNIPAM shell and air as the superstrate. Upon coating this AuNP lattice with a homogeneous film using spin-coating with a solution of linear PNIPAM homopolymer [23], we observe a strongly redshifted resonance at 617 nm with a rather narrow peak width of 40 nm (FWHM) shown by the spectrum in red in Fig. 7a.

Despite the narrow FWHM, this spectrum is also characterized by a small shoulder at a lower wavelength at approximately 540 nm that was not observed in the other two spectra. This shoulder is ascribed to a purely plasmonic contribution while the strong resonance at 617 nm is the result of plasmonic-diffractive coupling, i.e., a surface lattice resonance (SLR). This SLR is caused by the collective excitation of individual plasmons driven by an in-plane diffractive mode that is only enabled in a homogeneous RI environment [23, 45]. Due to the limited domain size and defects in the experimental lattice, the Q-factor $(Q = \lambda/\Delta\lambda)$ is limited and with a value of 15 rather small compared to lattices prepared by e-beam lithography, for example [46, 47].

Conclusion

Through the utilization of a fluid interface-assisted assembly and transfer methodology employing plasmonic core—shell microgels and substrates with varying wettability, we successfully prepared all five 2-dimensional Bravais lattices. Beginning with hexagonal arrangements of microgels at air/water interfaces, we achieved diverse lattice structures by strategically deforming the monolayer during transfer onto solid substrates. Notably, this deformation process was meticulously controlled solely by the wettability of the substrate, specifically its contact angle for water and the angle and speed of deposition onto the target substrate.

The resulting lattices exhibited a non-close-packed arrangement of plasmonic gold nanoparticles over extensive areas, showcasing pronounced long-range order with minimal local defects, as confirmed by advanced image analysis techniques. Plasmonic properties were comprehensively analyzed using extinction spectroscopy, revealing spectra that



Upon removal of the microgel shell via plasma treatment, a significant blueshift of the plasmon resonance was observed. Conversely, coating the non-close-packed array of gold nanoparticles with a thin but uniform polymer film resulted in a narrow and considerably redshifted resonance, identified as a surface lattice resonance arising from plasmonic-diffractive coupling in periodic plasmonic arrays with wavelength-scale interparticle distances.

This study builds upon our prior research focused on the assembly of rigid colloids, demonstrating the versatility of fluid interface-assisted assembly and transfer for soft colloid-like objects, specifically microgels. Furthermore, the utilization of core–shell microgels with plasmonic cores facilitated the formation of arrays comprising non-close-packed plasmonic nanoparticles. In light of recent endeavors to achieve complex tessellations from the (self-)assembly of soft colloids [48], our work not only expands the repertoire of reported structures but also underscores the potential for fabricating intricate, functional nanoparticle assemblies using core–shell building blocks.

Supplementary Information The online version contains supplementary material available at https://doi.org/10.1007/s00396-024-05285-4.

Acknowledgements The authors would like to acknowledge the Center for Advanced Imaging (CAi) at Heinrich-Heine University Düsseldorf for providing access to the SEM microscope ZEISS Supra 55VP and especially Steffen Köhler for performing the imaging. We would like to thank Jonathan Garthe for the assistance with the dip-coater and Philipp Hammers for providing the larger CS microgels.

Author contribution D.F. synthesized the core–shell microgels, prepared and characterized all monolayer samples, and performed the finite difference time domain simulations. M.O. performed the scanning and transmission electron microscopy measurements. M.S.D. computed the Voronoi and Delaunay tessellations and helped with the structural analyses and interpretation. D.F. wrote the initial manuscript. All authors have edited the manuscript. M.K. supervised and guided the project.

Funding Open Access funding enabled and organized by Projekt DEAL. The authors acknowledge the German Research Foundation (DFG) and the state of NRW for funding the cryo-TEM (INST 208/749–1 FUGG). M.K. acknowledges the DFG for funding under grant KA3880/6–1. D.F. acknowledges the Luxembourg National Research Fund (FNR), Project Reference 15688439. M.S.D. was supported by the U.S. Department of Energy (DOE), under award DE-SC0022229. This research was supported in part by grant NSF PHY-1748958 to the Kavli Institute for Theoretical Physics (KITP).

Availability of data and materials Data are available from the authors upon reasonable request. The Mathematica code used for image analysis (generation of Voronoi and Delaunay tessellations) is available from Zenodo and GitHub (https://doi.org/10.5281/zenodo.11974759).



Declarations

Ethical approval Not applicable.

Conflict of interest The authors declare no conflict of interests.

Open Access This article is licensed under a Creative Commons Attribution 4.0 International License, which permits use, sharing, adaptation, distribution and reproduction in any medium or format, as long as you give appropriate credit to the original author(s) and the source, provide a link to the Creative Commons licence, and indicate if changes were made. The images or other third party material in this article are included in the article's Creative Commons licence, unless indicated otherwise in a credit line to the material. If material is not included in the article's Creative Commons licence and your intended use is not permitted by statutory regulation or exceeds the permitted use, you will need to obtain permission directly from the copyright holder. To view a copy of this licence, visit http://creativecommons.org/licenses/by/4.0/.

References

- Vogel N, Retsch M, Fustin CA, del Campo A, Jonas U (2015) Advances in colloidal assembly: the design of structure and hierarchy in two and three dimensions. Chem Rev 115:6265–6311. https://doi.org/10.1021/cr400081d
- Vogel N, de Viguerie L, Jonas U, Weiss CK, Landfester K (2011) Wafer-scale fabrication of ordered binary colloidal monolayers with adjustable stoichiometries. Adv Funct Mater 21:3064–3073. https://doi.org/10.1002/adfm.201100414
- Goerlitzer ESA, Zhan MC, Choi S, Vogel N (2023) How colloidal lithography limits the optical quality of plasmonic nanohole arrays. Langmuir 39:5222–5229. https://doi.org/10.1021/acs.langmuir.3c00328
- Isa L, Buttinoni I, Fernandez-Rodriguez MA, Vasudevan SA (2017) Two-dimensional assemblies of soft repulsive colloids confined at fluid interfaces. Epl-Europhys Lett 119:26001. https:// doi.org/10.1209/0295-5075/119/26001
- Maier SA, Brongersma ML, Kik PG, Meltzer S, Requicha AAG, Atwater HA (2001) Plasmonics - a route to nanoscale optical devices. Adv Mater 13:1501–1505. https://doi.org/10.1002/1521-4095(200110)13:19%3c1501::AID-ADMA1501%3e3.0.CO;2-Z
- Romanov SG, Vogel N, Bley K, Landfester K, Weiss CK, Orlov S, Korovin AV, Chuiko GP, Regensburger A, Romanova AS, Kriesch A, Peschel U (2012) Probing guided modes in a monolayer colloidal crystal on a flat metal film. Phys Rev B 86:195145. https:// doi.org/10.1103/PhysRevB.86.195145
- Ai B, Yu Y, Möhwald H, Zhang G, Yang B (2014) Plasmonic films based on colloidal lithography. Adv Colloid Interfac 206:5–16. https://doi.org/10.1016/j.cis.2013.11.010
- Vogel N, Weiss CK, Landfester K (2012) From soft to hard: the generation of functional and complex colloidal monolayers for nanolithography. Soft Matter 8:4044–4061. https://doi.org/10. 1039/C1SM06650A
- Nemiroski A, Gonidec M, Fox JM, Jean-Remy P, Turnage E, Whitesides GM (2014) Engineering Shadows to fabricate optical metasurfaces. ACS Nano 8:11061–11070. https://doi.org/10.1021/ nn504214b
- Weekes SM, Ogrin FY, Murray WA, Keatley PS (2007) Macroscopic arrays of magnetic nanostructures from self-assembled nanosphere templates. Langmuir 23:1057–1060. https://doi.org/ 10.1021/la061396g

- Retsch M, Zhou ZC, Rivera S, Kappl M, Zhao XS, Jonas U, Li Q (2009) Fabrication of large-area, transferable colloidal monolayers utilizing self-assembly at the air/water interface. Macromol Chem Phys 210:230–241. https://doi.org/10.1002/macp.200800484
- Szekeres M, Kamalin O, Grobet PG, Schoonheydt RA, Wostyn K, Clays K, Persoons A, Dékány I (2003) Two-dimensional ordering of stöber silica particles at the air/water interface. Colloid Surface A 227:77–83. https://doi.org/10.1016/S0927-7757(03)00359-5
- van Baalen C, Vialetto J, Isa L (2023) Tuning electrostatic interactions of colloidal particles at oil-water interfaces with organic salts. Phys Rev Lett 131:128202. https://doi.org/10.1103/PhysRevLett. 131.128202
- Vogel N, Goerres S, Landfester K, Weiss CK (2011) A convenient method to produce close- and non-close-packed monolayers using direct assembly at the air-water interface and subsequent plasmainduced size reduction. Macromol Chem Phys 212:1719–1734. https://doi.org/10.1002/macp.201100187
- Hummel MEJ, Stelling C, Kopera BAF, Nutz FA, Karg M, Retsch M, Förster S (2019) Ordered particle arrays via a Langmuir transfer process: access to any two-dimensional Bravais lattice. Langmuir 35:973–979. https://doi.org/10.1021/acs.langmuir.8b03047
- Karg M, Pich A, Hellweg T, Hoare T, Lyon LA, Crassous JJ, Suzuki D, Gumerov RA, Schneider S, Potemkin II, Richtering W (2019) Nanogels and microgels: from model colloids to applications, recent developments, and future trends. Langmuir 35:6231– 6255. https://doi.org/10.1021/acs.langmuir.8b04304
- Nakahama K, Fujimoto K (2002) Thermosensitive two-dimensional arrays of hydrogel particles. Langmuir 18:10095–10099. https://doi.org/10.1021/la020541x
- Vialetto J, Nussbaum N, Bergfreund J, Fischer P, Isa L (2022) Influence of the interfacial tension on the microstructural and mechanical properties of microgels at fluid interfaces. J Colloid Interf Sci 608:2584–2592. https://doi.org/10.1016/j.jcis.2021.10.186
- Rey M, Fernandez-Rodriguez MA, Karg M, Isa L, Vogel N (2020) Poly-N-isopropylacrylamide nanogels and microgels at fluid interfaces. Accounts Chem Res 53:414

 424. https://doi.org/10.1021/acs.accounts.9b00528
- Scheidegger L, Fernández-Rodríguez MA, Geisel K, Zanini M, Elnathan R, Richtering W, Isa L (2017) Compression and deposition of microgel monolayers from fluid interfaces: particle size effects on interface microstructure and nanolithography. Phys Chem Chem Phys 19:8671–8680. https://doi.org/10.1039/ C6CP07896F
- Geisel K, Isa L, Richtering W (2012) Unraveling the 3D localization and deformation of responsive microgels at oil/water interfaces: a step forward in understanding soft emulsion stabilizers. Langmuir 28:15770–15776. https://doi.org/10.1021/la302974j
- Honold T, Volk K, Rauh A, Fitzgerald JPS, Karg M (2015) Tunable plasmonic surfaces via colloid assembly. J Mater Chem C 3:11449–11457. https://doi.org/10.1039/C5TC02115D
- Ponomareva E, Volk K, Mulvaney P, Karg M (2020) Surface lattice resonances in self-assembled gold nanoparticle arrays: impact of lattice period, structural disorder, and refractive index on resonance quality. Langmuir 36:13601–13612. https://doi.org/ 10.1021/acs.langmuir.0c02430
- Volk K, Fitzgerald JPS, Retsch M, Karg M (2015) Time-controlled colloidal superstructures: long-range plasmon resonance coupling in particle monolayers. Adv Mater 27:7332–7337. https://doi.org/ 10.1002/adma.201503672
- Volk K, Fitzgerald JPS, Ruckdeschel P, Retsch M, König TAF, Karg M (2017) Reversible tuning of visible wavelength surface lattice resonances in self-assembled hybrid monolayers. Adv Opt Mater 5:1600971. https://doi.org/10.1002/adom.201600971
- Karg M (2016) Functional materials design through hydrogel encapsulation of inorganic nanoparticles: recent developments



- and challenges. Macromol Chem Phys 217:242–255. https://doi.org/10.1002/macp.201500334
- Turkevich J, Stevenson PC, Hillier J (1951) A study of the nucleation and growth processes in the synthesis of colloidal gold. Discuss Faraday Soc. https://doi.org/10.1039/DF9511100055
- Rauh A, Honold T, Karg M (2016) Seeded precipitation polymerization for the synthesis of gold-hydrogel core-shell particles: the role of surface functionalization and seed concentration. Colloid Polym Sci 294:37–47. https://doi.org/10.1007/s00396-015-3782-6
- Kern W, Puotinen DA (1970) Cleaning solutions based on hydrogen peroxide for use in silicon semiconductor technology. Rca Rev 31:187–206
- Ebeling B, Vana P (2013) RAFT-polymers with single and multiple trithiocarbonate groups as uniform gold-nanoparticle coatings. Macromolecules 46:4862–4871. https://doi.org/10.1021/ma4008626
- Schneider CA, Rasband WS, Eliceiri KW (2012) NIH image to ImageJ: 25 years of image analysis. Nat Methods 9:671–675. https://doi.org/10.1038/nmeth.2089
- Johnson PB, Christy RW (1972) Optical constants of noble metals. Phys Rev B 6:4370–4379. https://doi.org/10.1103/PhysRevB.6. 4370
- Müller MB, Kuttner C, König TAF, Tsukruk VV, Förster S, Karg M, Fery A (2014) Plasmonic library based on substrate-supported gradiential plasmonic arrays. ACS Nano 8:9410–9421. https://doi. org/10.1021/nn503493c
- Brasse Y, Müller MB, Karg M, Kuttner C, König TAF, Fery A (2018) Magnetic and electric resonances in particle-to-film-coupled functional nanostructures. Acs Appl Mater Inter 10:3133–3141. https://doi.org/10.1021/acsami.7b16941
- Karg M, Jaber S, Hellweg T, Mulvaney P (2011) Surface plasmon spectroscopy of gold-poly-N-isopropylacrylamide core-shell particles. Langmuir 27:820–827. https://doi.org/10.1021/la1039249
- Dulle M, Jaber S, Rosenfeldt S, Radulescu A, Förster S, Mulvaney P, Karg M (2015) Plasmonic gold-poly(*N*-isopropylacrylamide) core-shell colloids with homogeneous density profiles: a small angle scattering study. Phys Chem Chem Phys 17:1354–1367. https://doi.org/10.1039/C4CP04816D
- Rauh A, Carl N, Schweins R, Karg M (2018) Role of absorbing nanocrystal cores in soft photonic crystals: a spectroscopy and SANS study. Langmuir 34:854

 –867. https://doi.org/10.1021/acs. langmuir.7b01595
- 38. Kuk K, Abgarjan V, Gregel L, Zhou Y, Carrasco Fadanelli V, Buttinoni I, Karg M (2023) Compression of colloidal monolayers at liquid interfaces: *in situ* vs. *ex situ* investigation. Soft Matter 19:175–188. https://doi.org/10.1039/D2SM01125E

- Volk K, Deißenbeck F, Mandal S, Löwen H, Karg M (2019) Moiré and Honeycomb lattices through self-assembly of hard-core/softshell microgels: experiment and simulation. Phys Chem Chem Phys 21:19153–19162. https://doi.org/10.1039/C9CP03116B
- Rauh A, Rey M, Barbera L, Zanini M, Karg M, Isa L (2017) Compression of hard core-soft shell nanoparticles at liquid-liquid interfaces: influence of the shell thickness. Soft Matter 13:158–169. https://doi.org/10.1039/C6SM01020B
- Haynes CL, McFarland AD, Zhao LL, Van Duyne RP, Schatz GC, Gunnarsson L, Prikulis J, Kasemo B, Käll M (2003) Nanoparticle optics: the importance of radiative dipole coupling in two-dimensional nanoparticle arrays. J Phys Chem B 107:7337–7342. https:// doi.org/10.1021/jp034234r
- Jenkins JA, Zhou YD, Thota S, Tian XD, Zhao XW, Zau SL, Zhao J (2014) Blue-shifted narrow localized surface plasmon resonance from dipole coupling in gold nanoparticle random arrays. J Phys Chem C 118:26276–26283. https://doi.org/10.1021/jp508181g
- Ghosh SK, Pal T (2007) Interparticle coupling effect on the surface plasmon resonance of gold nanoparticles: from theory to applications. Chem Rev 107:4797–4862. https://doi.org/10.1021/cr0680282
- Humphrey AD, Barnes WL (2014) Plasmonic surface lattice resonances on arrays of different lattice symmetry. Phys Rev B 90:075404. https://doi.org/10.1103/PhysRevB.90.075404
- Kravets VG, Kabashin AV, Barnes WL, Grigorenko AN (2018) Plasmonic surface lattice resonances: a review of properties and applications. Chem Rev 118:5912–5951. https://doi.org/10.1021/ acs.chemrev.8b00243
- Rodriguez SRK, Schaafsma MC, Berrier A, Rivas JG (2012) Collective resonances in plasmonic crystals: size matters. Physica B 407:4081–4085. https://doi.org/10.1016/j.physb.2012.03.053
- Kravets VG, Schedin F, Grigorenko AN (2008) Extremely narrow plasmon resonances based on diffraction coupling of localized plasmons in arrays of metallic nanoparticles. Phys Rev Lett 101:087403. https://doi.org/10.1103/PhysRevLett.101.087403
- Feller D, Karg M (2022) Fluid interface-assisted assembly of soft microgels: recent developments for structures beyond hexagonal packing. Soft Matter 18:6301–6312. https://doi.org/10.1039/ D2SM00872F

Publisher's Note Springer Nature remains neutral with regard to jurisdictional claims in published maps and institutional affiliations.

